Orientation and deformation conditions dependence of dislocation substructures in cold deformed pure tantalum

J. Baton, W. Geslin, Charbel Moussa

Orientation and deformation conditions dependence of dislocation substructures in cold deformed pure tantalum

J. BATON[a, *], W. GESLIN[b], C. MOUSSA[a]

[a]MINES ParisTech, PSL Research University, CEMEF - Centre de mise en forme des matériaux, CNRS UMR 7635, CS 10207 rue Claude Daunesse, 06904 Sophia Antipolis Cedex, France

[b]CEA DAM Valduc, F-21120 Is-sur-Tille, France

* Corresponding author.
E-mail address: jules.baton@mines-paristech.fr (J. Baton).

Abstract

The evolution of dislocation arrangement during deformation can lead to the development of dislocation substructures which have direct consequences on the subsequent microstructural evolutions. Dislocation densities and substructures of various deformed microstructures of pure tantalum are analyzed in order to study the influence of deformation conditions. Electron BackScatter Diffraction (EBSD) and Electron Channeling Contrast Imaging (ECCI) are used in order to characterize the development of dislocation substructures. Investigation at grain scale shows the orientation dependence of the deformed state with the highest dislocation content for γ-fiber grains. This fiber appears to be quite stable in compression but less in rolling. Investigation at dislocation substructure scale highlights the influence of orientation on dislocation substructure forming. Developed substructures are present in the interior of γ-fiber grains. The evolution of the disorientation and size of substructures with strain depends greatly on the initial fraction of γ-fiber in the microstructure. Models describing these evolutions are proposed for γ-fiber grains. On the basis of the present analysis it is concluded that dislocation density parameter does not allow transcribing the differences of substructural development.

Keywords

Tantalum; Cold deformation; Dislocation; Substructure; Crystallographic orientation; EBSD

1. Introduction

During cold deformation of a metallic alloy, a small amount of work (≈ 1%) is stored in the material and is correlated to generated dislocations [1]. This stored energy is the driving force for several thermally activated physical mechanisms during subsequent annealing such as recovery and recrystallization. These mechanisms determine the mechanical properties of the final part [2,3] therefore it is crucial to analyze and quantify the stored energy distribution in order to model recrystallization.

Tantalum is a bcc high density (16654 $kg.m^{-3}$) refractory metal (T_m = 2996°C) [4]. Thanks to its high ductility at room temperature, it can be employed to cold form parts with complex geometries with minimum damage risks. Pure tantalum and tantalum alloys have been used in many fields such as medical field, electronics or chemical industries for instance [5,6].

For body centered cubic (bcc) materials, three slip systems can be activated: {110} <111>, {112} <111> and {123} <111>, all three having the same slip direction giving dislocations the possibility to move from one slip plane to another [7]. The activation of those slip systems depends on deformation temperature, strain rate, chemical composition and crystal orientation [1,7]. For Ta, it was generally observed that even though slip activity is mainly on {110} planes, it is also present on plane with maximal resolved shear stress [8]. Moreover, stacking faults have been rarely observed experimentally for bcc materials and the computation of energy with voluntarily created stacking faults has confirmed that stable faults are unlikely to exist. Therefore, the stacking fault energies are often estimated only theoretically with some assumptions [9,10]. The ease of cross slip suggests a very similar dislocation behavior to high stacking faults face centered cubic (fcc) materials [7] such as aluminum. With cross slip ability, dislocations tend to form well-organized substructures during plastic deformation.

Due to the micrometer range of substructures, Transmission Electron Microscopy (TEM) is mostly used to characterize microstructures. Size and shape of substructures were mainly studied in deformed fcc metals such as Al [11–14], Ni [15,16], Cu [14,17] or austenitic 304L stainless steel [15]. Results have shown the decrease of substructure size with increasing strain. The work of Gil Sevillano et al. [18] revealed that a wide range of materials displayed a similar behavior including bcc materials and experiments on cold worked Nb [19] and iron [20] have confirmed this observation. The evolution of the substructure disorientation with deformation has also been investigated but to a lesser extent. Some studies on this topic have been carried out on bcc materials such as iron [18,20] but most of the investigations have been realized once again on fcc materials in particular on Al [11–14,21,22]. It has been

found that generally the substructure disorientation increased with strain. An attempt to determine a universal behavior of dislocation substructures has been done. For that purpose, substructures boundaries, also named subboundaries, were classified in two different types [23]: Incidental Dislocation Boundaries (IDBs) and Geometrically Necessary Boundaries (GNBs). Pantleon and Hansen [24] demonstrated that the disorientation distribution of dislocation boundaries can be described with a Rayleigh function of IDBs and GNBs. Pantleon [25] demonstrated that the saturation of boundaries disorientations frequently observed is an artefact due to both the threshold disorientation angle used to differentiate dislocations boundaries from grain boundaries and the superposition of IDBs and GNBs.

Electron Back Scatter Diffraction (EBSD) technique has emerged in the last decades and became a powerful tool to characterize microstructures. Although the limiting factor of EBSD concerning its angular resolution (≈ 0.5°), this technique provides data of much better statistical relevance than TEM data thanks to bigger analyzed surfaces. Therefore, a quantitative characterization of dislocation substructures on larger scales is achievable. Similarly to TEM studies, pure Al and Al alloys deformed microstructures have been intensively characterized with EBSD technique [26–29]. The observed evolutions of substructure size and disorientation were consistent with TEM observations. Less investigations on bcc metals such as pure Nb [30] or pure Ta [31,32] have been generally carried out but have also reported similar results.

The influence of crystallographic orientation on grain deformation has been also a topic extensively under investigation. In order to have a better understanding of the recrystallization texture, Dillamore et al. [33] observed with TEM technique that substructure size and disorientation were orientation dependent for cold rolled iron. Substructure size decreased and disorientation increased as the rolling plane of the grains rotated from {001} to {110} around the rolling direction <110>. Similar orientation dependence for the stored energy has been found on rolled steel using a X-ray line broadening method [34] and more recently on cold worked high purity iron using a high resolution X-ray method [35]. Orientation dependence of substructure development has been also observed for fcc metals such as for rolled pure Al [36] characterized with TEM technique where the substructures properties evolved differently depending on the considered rolling texture component. Complementary information on the deformation substructures have been found with EBSD investigations for instance on Al alloy [28] where it has been shown that the crystallographic orientation influenced mainly the substructure disorientation but not much their size. For the specific case of pure Ta, this influence has been also studied and the work of Sandim et al. [37] on cold rolled coarse-grained high-purity Ta has clearly illustrated it with two grains with different substructure development: one grain subdivided into regions with a large range of

disorientations whereas the other one deformed in a more stable way with low misoriented subboundaries. Moreover, EBSD investigations on cold rolled pure Ta [38–40] have shown that more generally grains with the direction <111> parallel to the normal direction of the sheet contained more substructures and had a higher stored energy, quantified with the quality of EBSD patterns, than grains with the direction <100> parallel to the normal direction.

Although these previous studies have indicated that individual grains behaved quite differently during the deformation because of crystallographic orientation, existing literature has not reported quantitative characterization of the evolution of the spatial distribution of substructures with strain for pure Ta. Indeed, not only the disorientation of substructures is of interest but also the spatial organization of the substructures has to be studied because it can impact the subsequent annealing mechanisms. For instance, Yu et al. [41] have found that the triple junction formed by the substructures in cold rolled Al may act on recovery and on recrystallization. The triple junction motion during recovery allowed a structural coarsening and the formed equiaxed structures might represent possible nuclei for recrystallization.

In the current investigation, the evolution of dislocation substructures during room temperature plastic deformation is investigated in pure Ta. Samples were deformed by uniaxial compression and rolling. An investigation of the orientation dependence of dislocation content and dislocation substructure development is performed. Two scales of observation with the EBSD technique are used in order to characterize the deformed microstructures. Firstly, at grain scale to examine the evolution of the texture and of the dislocation density with increasing strain. Secondly, at dislocation substructure scale to observe and quantify with a lower resolution the spatial distribution and development of substructures. Correlations between macroscopic and microscopic observations are then discussed. Parameters to quantify substructure development are defined and models for its evolutions with strain are proposed.

2. Material preparation and SEM characterization

For microstructural analysis, surfaces were prepared by mechanical polishing up to 4000 grit SiC paper. Several papers were used for each step to ensure the removal of the hardened layer of the previous step and not simply erase the previous scratches. A chemical-mechanical polishing was then performed with a colloidal silica suspension with an average

particle diameter of 20 nm. The samples were finally etched with a solution of 25% HF and 75% HNO_3 for several seconds.

EBSD scans were performed on a Carl Zeiss Supra40 Field Emission Gun Scanning Electron Microscope (FEG-SEM) operated under 20 kV with a Bruker Quantax system comprising a FlashHR EBSD detector and the Esprit 2.1 EBSD software package. EBSD maps were acquired at the samples mid-thickness. For intergranular observations, an acquisition step size of 1.20 µm was used over a rectangular area of 1.20 mm × 0.90 mm. This measurement step size was chosen to achieve a compromise between the measurement area and the spatial resolution in order to have statistically relevant data. For intragranular observations, EBSD maps with an acquisition step size of 90 nm were performed in the interior of the grains. This measurement step size allows the distinction of close dislocation subboundaries even in the most deformed cases. For EBSD data treatments, MTEX toolbox was used [42]. Electron Contrast Channeling Imaging (ECCI) micrographs under 30 kV with a backscatter electron detector were also performed at this scale for a direct observation of dislocation substructures.

3. Initial state

The as-received material is a sheet of 12 mm thickness of pure tantalum (> 99.99% wt) that was subject to cold rolling then to a recrystallization heat treatment. The initial fully recrystallized microstructure exhibits heterogeneities between the center and the quarter layer (3 mm from the center) of the sheet as illustrated in Fig. 1. In order to study texture evolutions, grains were classified into the following three groups based on their average orientations: the θ-fiber grains with <100> parallel to the normal direction of the sheet (ND)[1], the γ-fiber grains with <111> parallel to ND and the “other” grains which refers to any grain not belonging to the two previous fibers. A 15° tolerance was used to perform this classification.

The γ-fiber is very intense at the center of the sheet (approximately 81% in grain surface fraction in Fig. 1a and see also the high intensity in {111} pole figure of Fig. 1c). For the microstructure in the quarter layer, the distribution of orientations is more homogeneous with a weaker γ-fiber and a stronger θ-fiber as illustrated in Fig. 1b and 1d. This variation of

[1] The initial sheet was received in the form of a disc and the direction of the last rolling pass is unknown. The samples being taken from different locations on the sheet, the Radial Direction RD and the Transverse Direction TD are only indicative. On the other hand, ND stands for the real macroscopic normal direction of the initial sheet and is common to all the samples. Therefore, it is the reference direction used for all this study.

orientation can be attributed to the last stage of cold rolling before the recrystallization treatment in the sheet forming process. Indeed, as observed both on bcc and fcc metals [43,44], the effect of friction between the rolls and the sheet during cold rolling can induce shear components near the sheet surface and then leads to through-thickness texture heterogeneities.

The two observed microstructures show also a difference of grain size with larger grains in the center than in the quarter layer, i.e. 156 µm and 108 µm for the average equivalent diameter weighted by surface respectively (grains on the edges of EBSD maps were not included in the calculation of grain sizes). Grains with an area smaller than 5 pixels were excluded from analysis and the threshold disorientation angle of 10° was considered to define grain boundaries.

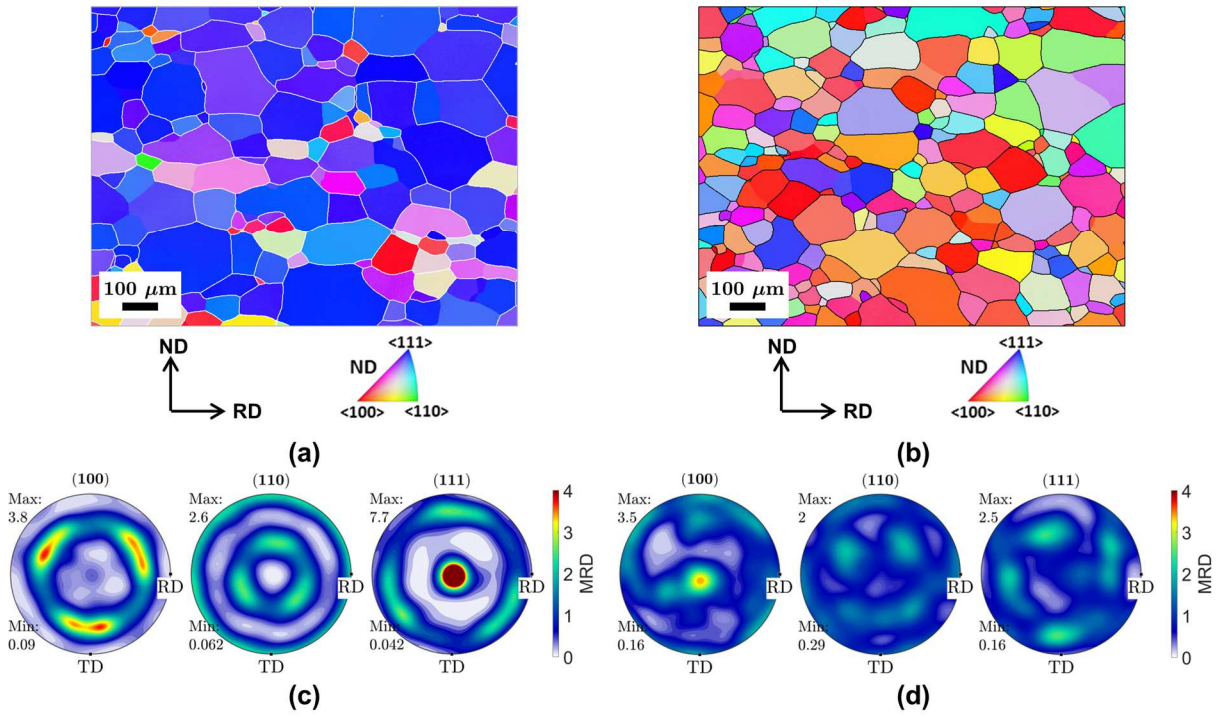

Fig. 1. Electron Back Scatter Diffraction (EBSD) orientation maps of the as-received material for (a) the center of the sheet (samples used for compression) and (b) the quarter layer at 3 mm from the center (samples used for rolling) (Normal Direction ND projected onto the standard triangle; RD: Radial Direction). Grain boundaries are plotted in white and black lines for the center and the quarter layer of the sheet respectively (10° disorientation angle threshold). (c) and (d) corresponding pole figures for the two locations respectively (TD: Transverse Direction).

In order to have a macrotexture information of the initial state, an X-ray diffraction instrument (Panalytical® X'Pert^3) with Cu Kα radiation (45 kV/30 mA) was used at the center and at the

quarter layer of the sheet in the RD-TD (transverse direction) plane. Pole figures of {110}, {200}, {211} and {222} were measured with a tilt angle from 0° to 69° with a step size of 3°. The orientation distribution functions (ODFs) were calculated from the above four poles figures using the MTEX toolbox [42] taking into account the noise effect and the ghost problem. As bcc materials often exhibit fiber textures after cold rolling or recrystallization, it is usual to represent the ODFs in the Euler space, in particular in the section $\varphi_2 = 45°$ where θ-fiber and γ-fiber can be found as illustrated in Fig. 2c [1]. The macrotexture acquired at the center and at the quarter layer of the initial sheet are shown in Fig. 2a and 2b respectively. Results confirm the difference of texture between these two locations previously observed with the EBSD technique in Fig. 1c and 1d. {111} <110> orientations of γ-fiber appear to be very predominant at the center whereas {001} <100> and {001} <110> orientations of θ-fiber prevail at the quarter layer but in a lesser extent with more uniformly distributed orientations. Moreover, the macrotexture obtained by XRD technique can be compared quantitatively to the microtexture obtained by EBSD technique as shown in Fig. 2d. For the quarter layer the two techniques display similar results concerning the fraction of each class of orientations. For the center more differences can be seen, in particular for the γ-fiber with a weaker fraction with the XRD technique (≈ 18% less). This difference can result from the statistical relevance depending on the used technique or from spatial heterogeneities of texture in the initial sheet. As shown in Appendix A with EBSD maps ten times larger than the ones of Fig. 1, the dominance of the γ-fiber can vary by more than 10% depending on the position at the center of the sheet. This variation can explain the difference observed between XRD and EBSD results. Therefore, as these two techniques give close trends concerning the texture, only the EBSD technique is used in the following.

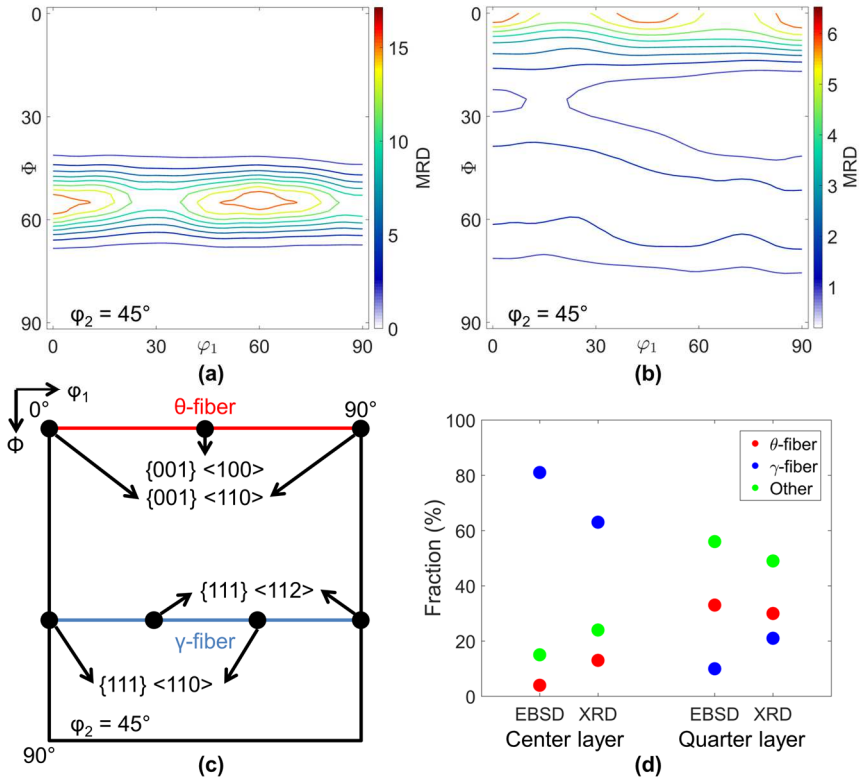

Fig. 2. ODF sections ($\varphi_2 = 45°$) for (a) center and (b) quarter layers of the initial sheet; (c) location of fibers and main texture components found in the section $\varphi_2 = 45°$ of the Euler space; (d) comparison of fraction of each class of orientations between EBSD (grain surface fraction) and XRD techniques for center and quarter layers.

4. Deformed microstructure

4.1. Deformation conditions

Cold rolling and uniaxial compression tests were performed in order to study deformed microstructures. For both deformation modes, parallelepipeds were taken from the initial sheet at different locations as illustrated in Fig. 3a. For compression tests, samples were machined in the total thickness of the parallelepipeds. Therefore, the initial state of the compressed samples at the center is the one presented in Fig. 1a. The compression direction CD is parallel to the normal direction ND of the initial sheet. In order to obtain a strain gradient in one sample, two double-cone geometries, presented in Fig. 3b, were chosen. The von Mises equivalent plastic strains (ε_{VM}) of the deformed samples were determined using finite elements simulation with Forge® software as illustrated in Fig. 3c. The constitutive laws used were taken from the work of Kerisit [45]. For the friction between the tools and the sample, a Tresca law was used with a friction coefficient of 0.4, determined by minimizing the difference of geometrical bulge between experimental and simulated

compression on cylinder. The two geometries used for this study lead to a ε_{VM} that ranges from 0.05 to 0.65 and from 0.15 to 1.09 respectively. The geometry 1 enables the observation in detail of low strain case and higher strains can be reached with the geometry 2.

For cold rolling, parallelepipeds were taken from the initial sheet and cut into two identical halves (Fig. 3a). The obtained halves of around 5.9 mm thickness were used as samples for rolling. Therefore, the initial state of the rolled samples at the center is the one presented in Fig. 1b. The normal and the rolling directions of the rolling are parallel to the normal direction ND and to the radial direction RD of the initial sheet respectively. With a 54 mm diameter rolling mills and a rotation speed of 4 m/min five samples were cold rolled in several passes (0.05 mm per pass) with lubricated rolls. Five different total thickness reductions of 38%, 45%, 58%, 68%, and 76% were obtained, resulting in five von Mises equivalent plastic strains (ε_{VM}) respectively of 0.56, 0.70, 1.00, 1.33, 1.67 [46]. The ratio of the contact length between the rolls and the sheet, l_c, to the sheet thickness, d, was kept between 1 and 5 to ensure homogeneous deformation [44,47]. Moreover, a systematic rotation of the sample of 180° along the transverse direction was performed between the rolling passes.

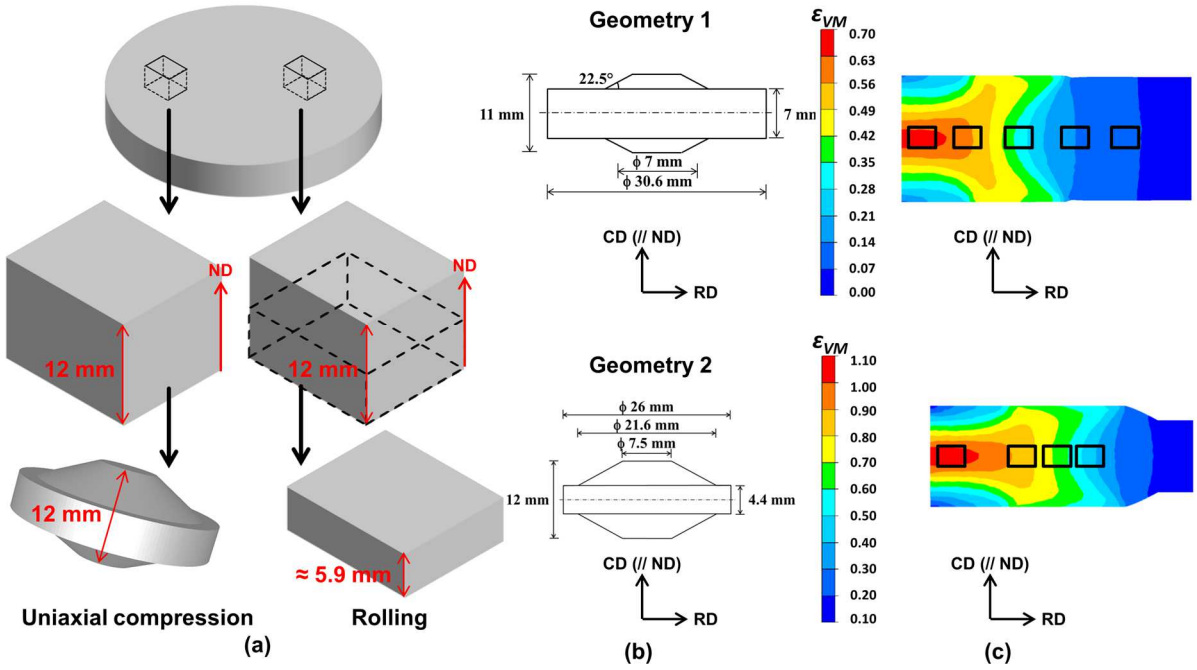

Fig. 3. (a) Sketch representing where the samples for compression and rolling are taken from the as-received sheet; (b) double-cone sample geometries; (c) ε_{VM} in the CD-RD plane after compression (CD: Compression Direction and RD: Radial Direction). Note that CD is the ND of the initial sheet. Black rectangles show examined regions with SEM.

Deformed microstructures were characterized in terms of texture evolution and dislocation substructure development in the following sections. Observations are discussed in light of the difference of texture between the initial states of compressed and rolled samples and not in light of the difference of deformation mode. The influence of deformation mode is beyond the scope of this paper.

4.2. Texture evolution

EBSD maps of samples deformed by compression, with geometry 1 and 2 (Fig. 3b), and by rolling are presented in Appendices B, C and D respectively. The respective evolutions of θ-fiber, γ-fiber and "other" orientations with strain are detailed quantitatively for the compressed and for the rolled samples in Fig. 4a and 4b respectively.

For both geometries of compression samples, the γ-fiber remains stable and very intense with strain. For geometry 1 samples, the surface fraction of γ-fiber grains is around 90% for all studied strains with a maximum of 96% for the highest strain. For geometry 2 samples, the surface fraction of γ-fiber grains is around 65% and of θ-fiber grains around 20% for all strains. In both cases, plastic deformation does not seem to modify the crystallographic texture. The difference between the two cases is attributed to the initial state where the dominant γ-fiber is present between 70% and 80% depending on the location of EBSD maps as illustrated in section 3 and Appendix A. The observations made in Fig. 4a and the stability of the γ-fiber during uniaxial compression are consistent with the formation of fiber textures regularly found for bcc materials [48,49].

In the case of rolled samples, more variations of texture were observed. In the initial state the γ-fiber and the θ-fiber represent around 10% and 30% respectively as shown in Fig. 4b. For $\varepsilon_{VM} \approx 0.56$, the γ-fiber is more intense and this can be surely related to the compression components at the center of the sheet. Above this strain, the intensity of γ-fiber continuously decreases with strain to the benefit of the two other classes of orientations, in particular the "Other" one which reaches more than 50% of the total surface. This decrease was also reported on previous experiment on pure Ta [50] and can be attributed to the same effect of friction between the rolls and the sheet already observed on starting material. Indeed, the superposition of added shear components to already present compression components might lead to a more randomized texture [43,44]. For small reductions, this effect is restricted to a layer near the surface and with increasing reduction it impacts deeper layers. For example, for $\varepsilon_{VM} \approx 1.33$ and 1.67 the thickness of the samples is 1.9 mm and 1.4 mm respectively. Considering the width of EBSD maps (0.9 mm), a larger part of the

characterized surface contains zones impacted by the friction which tends to decrease the intensity of γ-fiber and randomizes the texture. Furthermore, it can be noted that the α-fiber, another fiber generally composing the texture of cold rolled bcc materials [1,50], remains quite stable during rolling in the present case with a surface fraction of α-fiber grains between 32% and 46%.

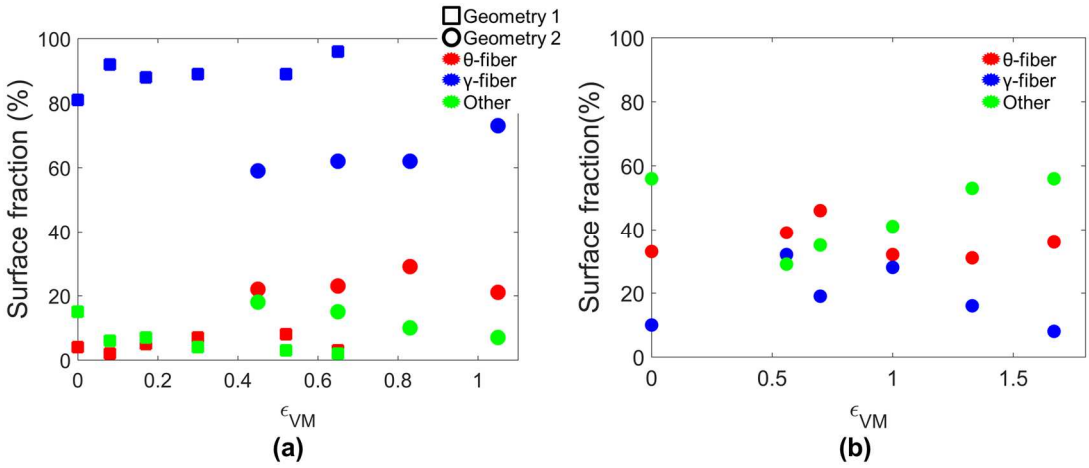

Fig. 4. Evolution of θ-fiber, γ-fiber and "other" orientations with strain for (a) compressed samples and (b) rolled samples.

4.3. Deformation induced grain subdivision

4.3.1. Intergranular analysis

Ashby's classification distinguishes Statistically Stored Dislocations (SSDs) from Geometrically Necessary Dislocations (GNDs) [51]. These two types have a distinct nature. SSDs are created under homogeneous plastic deformation and do not imply orientation gradient whereas GNDs are created for the accommodation of heterogeneous plastic deformation and imply significant orientation gradient. As SSDs are redundant whereas GNDs are not, the acquisition step size and the technique resolution for the orientation measurement affects the distinction between them. Indeed, depending on the step size, dislocation may be considered redundant or not. Hence, the use of a physically based classification (SSDs and GNDs) to define quantities that are mainly distinguished by scale effects and step size choice may be misleading. Therefore, dislocation densities estimated from EBSD data are defined in the present paper as ρ_{EBSD}. In this paper, the method proposed by Pantleon [52] and implemented by Seret et al. [53] was used. This method is based on the continuum theory of dislocations with the determination of the Nye's tensor [54]. In order to avoid any misinterpretation that can be linked to the hypothesis of the used

method to estimate ρ_{EBSD}, the disorientation angle per segment θ_s was used as a second parameter to quantify intragranular disorientations induced by dislocation content [55]. This parameter is the disorientation angle of each pair of adjacent pixels horizontally and vertically on the overall EBSD map and the average value is then calculated.

Using the EBSD maps presented in Appendices B, C and D, ρ_{EBSD} and θ_s were calculated. For the compressed samples, the evolutions of $\overline{\rho_{EBSD}}$ and $\overline{\theta_s}$ with strain are presented in Fig. 5a. In the starting material, $\overline{\rho_{EBSD}}$ and $\overline{\theta_s}$ were determined as 9.7x10^{13} m^{-2} and 0.4° respectively. As the material was deformed, the dislocation content quickly increases and then seems to be saturating for further deformation with a plateau reaching 1.3×10^{15} m^{-2} and 2.9° for $\overline{\rho_{EBSD}}$ and $\overline{\theta_s}$ respectively. Besides, the trend appears to be qualitatively similar for both parameters.

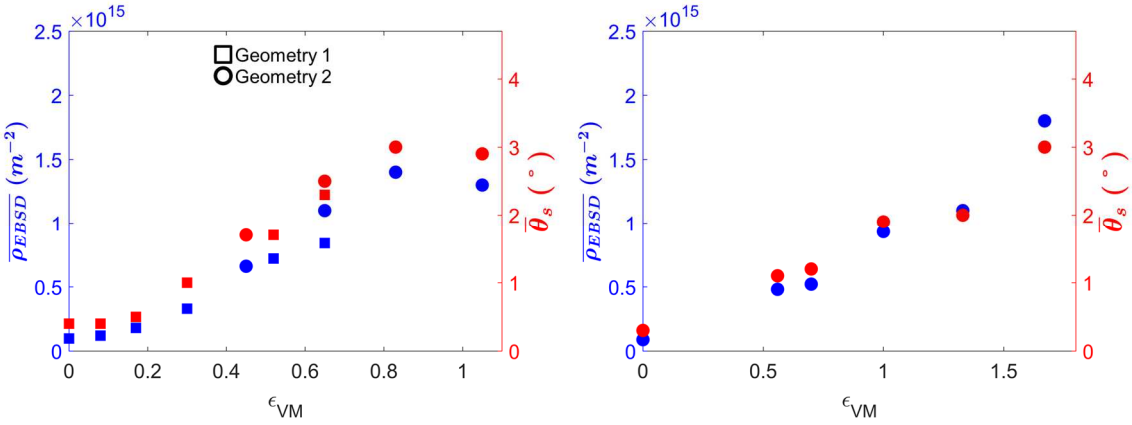

Fig. 5. Evolution of $\overline{\rho_{EBSD}}$ and $\overline{\theta_s}$ with strain for (a) compressed samples and (b) rolled samples.

For the rolled samples, the evolutions of $\overline{\rho_{EBSD}}$ and $\overline{\theta_s}$ with strain are presented in Fig. 5b. Similarly to the compression case these values increase with deformation as expected, but no apparent saturation is observed for this case. It is worth noticing that the increase in the case of rolling (Fig. 5b) is slower than in the case of compression (Fig. 5a). This difference is probably induced by the differences in the crystallographic orientations. Indeed, for the case of compression, the material at the initial state has between 70% and 80% of γ-fiber grains. On the contrary, for the case of rolling the material at the initial state has around 10% and 30% of γ-fiber and θ-fiber grains respectively. Therefore, the evolutions of $\overline{\rho_{EBSD}}$ and $\overline{\theta_s}$ with strain depend on the crystallographic orientation. To examine this influence, all the pixels of grains belonging to each class of orientations are gathered and then $\overline{\rho_{EBSD}}$ and $\overline{\theta_s}$ are calculated for each class independently. As $\overline{\rho_{EBSD}}$ and $\overline{\theta_s}$ gave similar results for the compression and the rolling cases, the study of the orientation effect is depicted only with $\overline{\rho_{EBSD}}$ in the following. The evolutions of $\overline{\rho_{EBSD}}$ with strain for θ-fiber, γ-fiber and "other"-

oriented grains are shown in Fig. 6a and the distributions of ρ_{EBSD} for each class of orientations are presented in Fig. 6b and 6c for $\varepsilon_{VM} \approx 0.56$ and 1.67 respectively. The evolution of the dislocation content differs between each class of orientations. $\overline{\rho_{EBSD}}$ is higher for the γ-fiber grains than for the θ-fiber grains of approximately 60% and the increase seems also faster for the γ-fiber grains. Moreover, the distributions appear also to be wider for the γ-fiber grains with a shift to the right with increasing strain, illustrating a distinct intragranular behavior between these two fibers. These results are consistent with the numerous investigations on the influence of crystallographic orientation on deformation performed on bcc materials such as Fe [33,35], steel [34,56] or Ta [37–39,57] for instance.

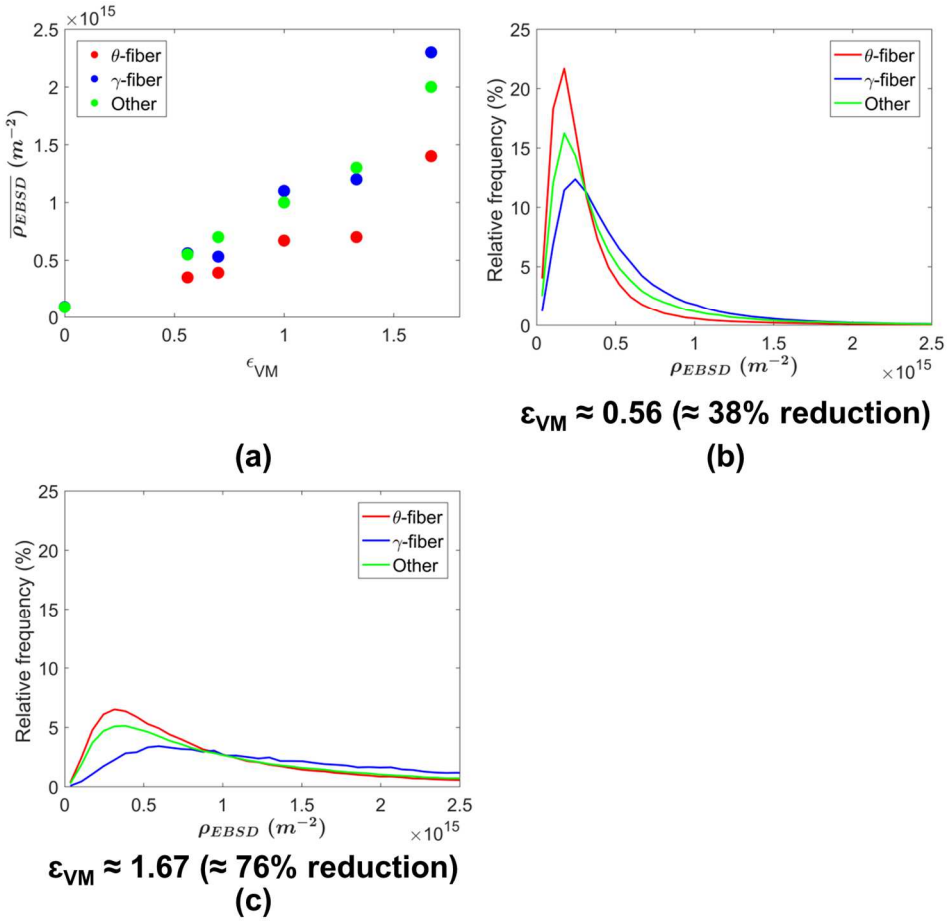

Fig. 6. (a) Evolution of $\overline{\rho_{EBSD}}$ with strain for each class of orientations; distribution of ρ_{EBSD} for each class of orientations for $\varepsilon_{VM} \approx$ (b) 0.56 and (c) 1.67.

As it can be observed in Fig. 5a and Fig. 5b, the evolutions of $\overline{\rho_{EBSD}}$ are different between the compression case and the rolling case. However, when only the γ-fiber grains are considered, the difference between these two evolutions is lower at the studied scale as presented in Fig. 7. Despite this observation at the macroscopic scale, the behavior of the γ-fiber grains at the dislocation substructure scale is very different between these two cases as illustrated later in the following section.

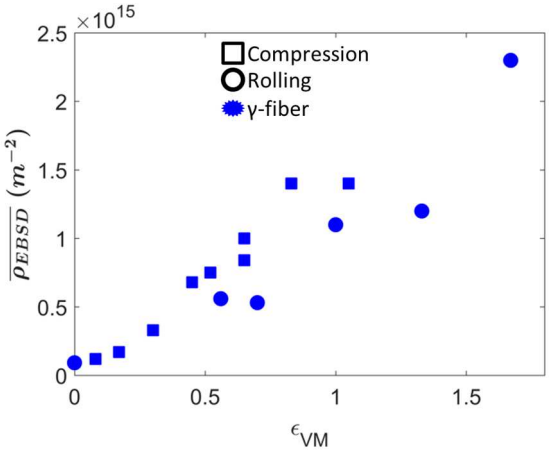

Fig. 7. Evolution of $\overline{\rho_{EBSD}}$ with strain for compressed samples (the two geometries are taken together) and rolled samples for the γ-fiber grains.

The Taylor factor describes the slip systems activity during plastic deformation and is related to the amount of work required to deform grains for a given strain. As it is quite difficult to determine which specific slip system is activated for each grain, the typical slip systems for bcc materials [1] are employed for the calculation of the Taylor factor ({110} <111>, {112} <111>, {123} <111>) and it is assumed that the critical resolved shear stress is the same for all slip systems. The calculation is performed with the MTEX toolbox [42]. The Taylor factor for the γ-fiber, the θ-fiber and "other"-oriented grains are 3.5, 2.4 and 3 respectively. Those values are in agreement with the previous disparities of $\overline{\rho_{EBSD}}$ between the three sets of grains (Fig. 6a) highlighting the difference of behavior during plastic deformation. However, when each grain is considered separately no direct correlation between the Taylor factor and $\overline{\rho_{EBSD}}$ was observed for none of the deformed states as reported for $\varepsilon_{VM} \approx 1.00$ in Fig. 8. Weak and partial correlations between the Taylor factor and the dislocation content have previously been reported [58–60]. On the basis of those observations, the Taylor factor can explain global trends between each class of orientations but is not relevant to predict the intragranular deformation of grains. Indeed, the local boundary conditions on each grain are different from the macroscopic ones because of the different neighboring grains' behavior.

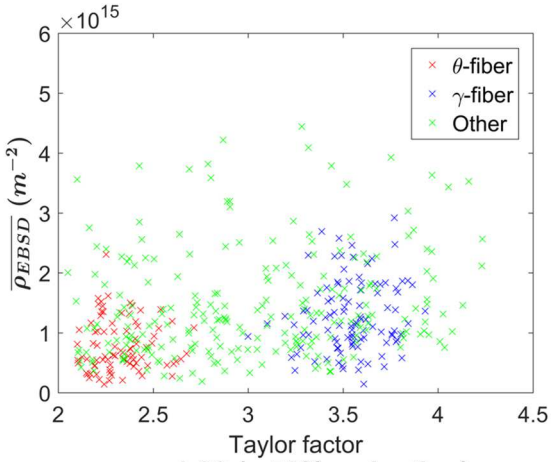

ε_{VM} ≈ 1.00 (≈ 58% reduction)

Fig. 8. $\overline{\rho_{EBSD}}$ per grain vs Taylor factor plot for rolled sample for ε_{VM} ≈ 1.00.

4.3.2. Dislocation substructures analysis

The deformed microstructures were observed at a lower scale to analyze the dislocation substructures. A first direct qualitative observation was realized with the ECCI technique with a specific investigation on the θ-fiber and the γ-fiber grains. ECCI micrographs performed in the interior of the grains in compressed and rolled microstructures are shown in Fig. 9 and 10 respectively.

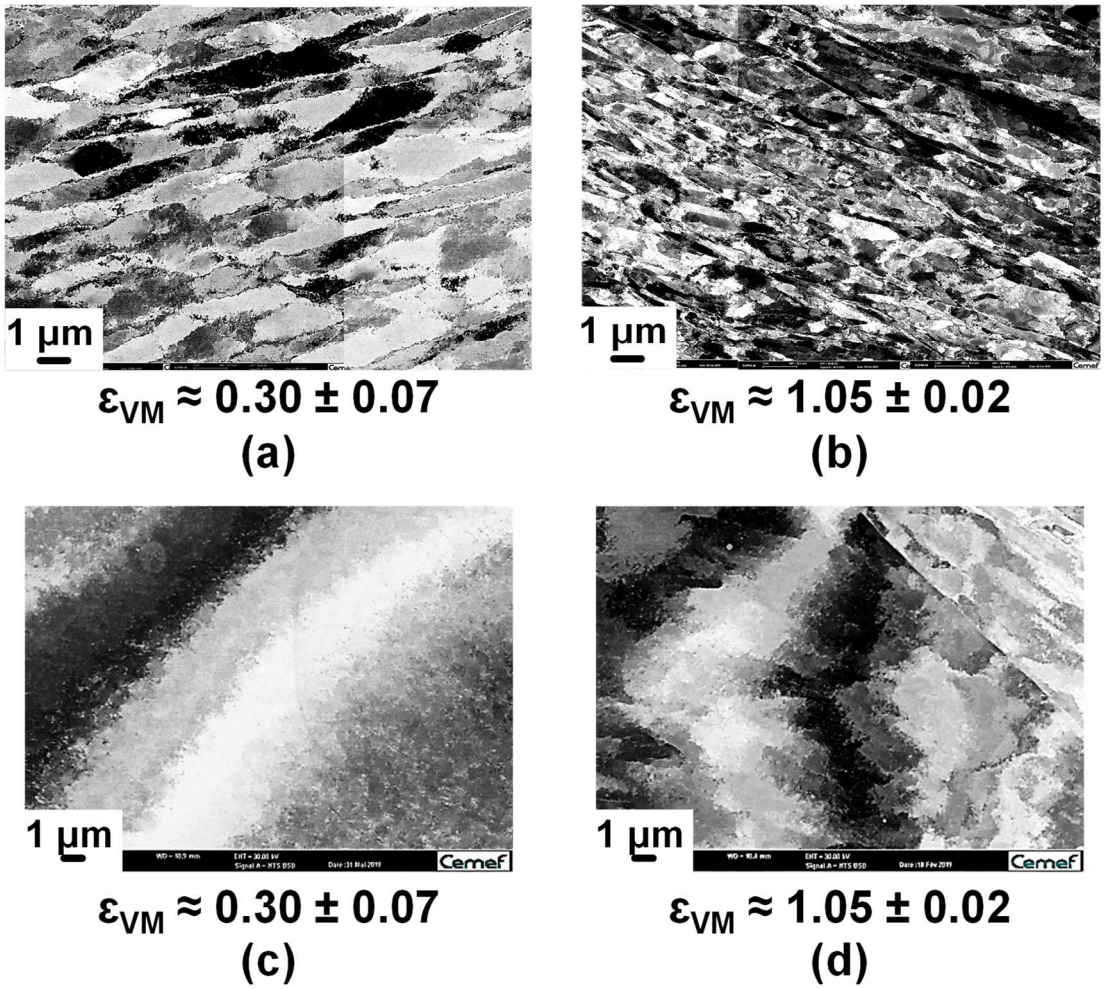

385

386 Fig. 9. ECCI micrographs on (a) & (b) γ-fiber grains and (c) & (d) θ-fiber grains for $\varepsilon_{VM} \approx 0.30$
387 and 1.05 respectively for compressed samples (the compression direction is vertical).

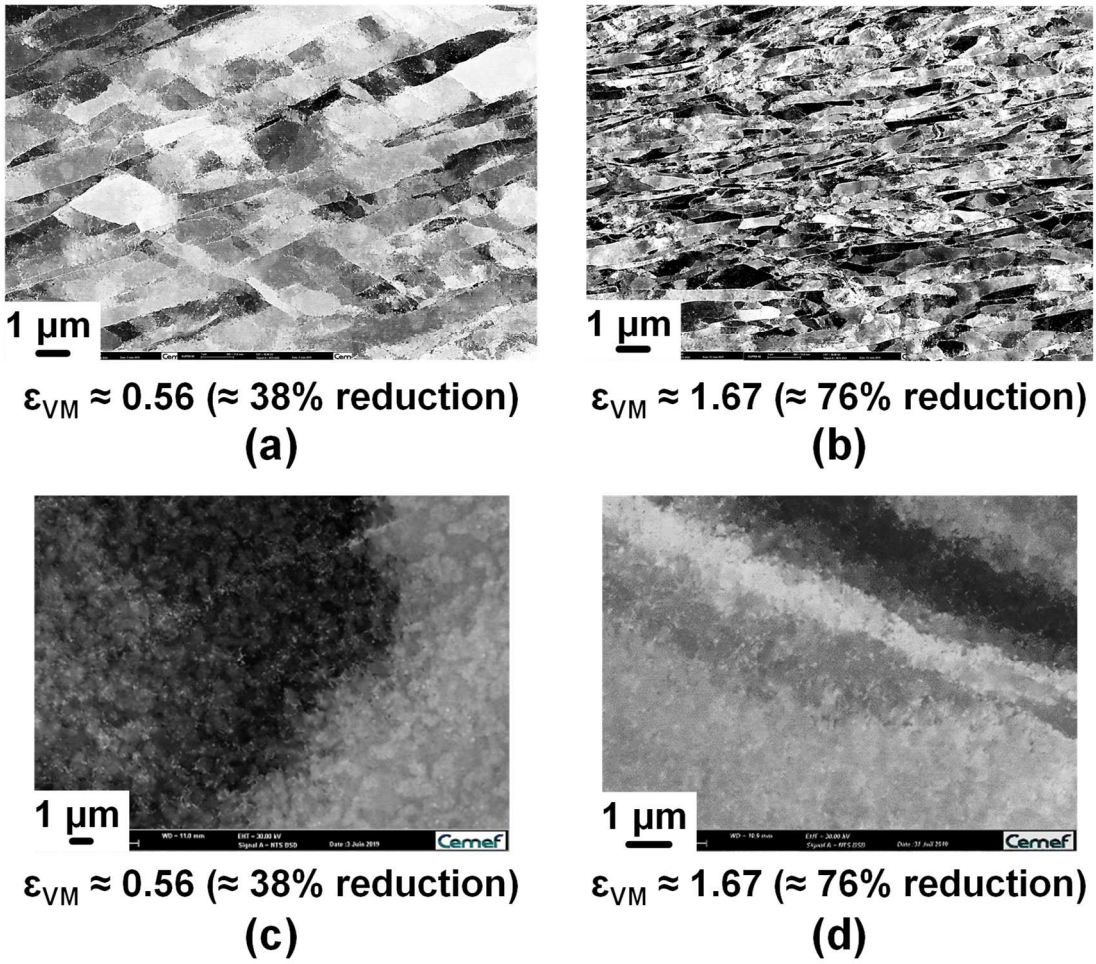

Fig. 10. ECCI micrographs on (a) & (b) γ-fiber grains and (c) & (d) θ-fiber grains for $\varepsilon_{VM} \approx 0.56$ and 1.67 respectively for rolled samples (the rolling normal direction is vertical).

For the two cases, there is a distinct substructure development between the two fibers. For the γ-fiber grains (Fig. 9a and b and Fig. 10a and b) dislocation substructures are well defined even for the smallest deformation $\varepsilon_{VM} \approx 0.30$. For small strains (Fig. 9a and 10a) evidence of dislocations entanglement can be observed in the subboundaries and there are some traces of dislocations inside subgrains. For high strains (Fig. 9b and 10b) thinner subboundaries are better defined and less traces of dislocations inside subgrains are observed. In addition, the subgrain size is observed to decrease with increasing strain which is in coherence with previous results as reported in section 1. For the rolled samples (Fig. 10a and b) the subboundaries look also gradually more aligned parallel to the rolling direction with increasing strain which is consistent with previous investigations on Al and Ni [22,28,36].

For the θ-fiber grains (Fig. 9c and d and Fig. 10c and d) no dislocation substructures can be observed even for the highest strain $\varepsilon_{VM} \approx 1.67$ with just few developed subboundaries. This observation is in agreement with the orientation dependence of intragranular heterogeneities

noticed previously at larger scale (section 4.3.1). It can be concluded that even if $\overline{\rho_{EBSD}}$ of θ-fiber grains increases with strain (Fig. 6a), this increase does not involve sharper substructure development. Therefore, the evolution of the dislocation content and their spatial distribution within substructures are different between the θ-fiber and the γ-fiber grains.

EBSD maps with an acquisition step size of 90 nm were performed in the interior of the grains to investigate quantitatively the dislocation substructures. Acquisitions were done the most possible at the center of grains to have results more representative to the crystallographic orientation and less affected by the proximity to grain boundaries. In order to have statistical relevance, EBSD maps were acquired on several grains for each strain level and for each class of orientations. Only the γ-fiber grains were investigated for the compression case because of the very high intensity of this fiber. The number of examined grains and the total surface observed with EBSD for each case are summarized in Table 1. The segments with a disorientation angle between 1.5° and 10° are considered to be induced by dislocation subboundaries and so are denoted as θ_{sub}. In order to describe the substructure development, two parameters were employed: the average disorientation angle of subboundaries $\overline{\theta_{sub}}$ (°) and the average linear density of subboundaries $\overline{\rho_{sub}^{l}}$ (μm^{-1}). The latter is calculated with the division of the sum of subboundary length by the total observed surface.

Table 1: Number of examined grains and total surface observed with EBSD for the observation at dislocation substructure scale.

Deformation mode	Strain level (ε_{VM})	Class of orientations	Number of examined grains	Total surface observed with EBSD (µm²)	Average estimated orientation gradient (°/µm)
Compression	0.30	γ-fiber	6	21891	0.07
	0.65	γ-fiber	6	17602	0.12
	1.05	γ-fiber	8	24177	0.17
Rolling	0.56	θ-fiber	2	2990	0.23
	1.00	θ-fiber	2	2256	0.28
	1.33	θ-fiber	4	6957	0.45
	1.67	θ-fiber	4	2080	0.91
	0.56	γ-fiber	5	15037	0.22
	1.00	γ-fiber	6	9278	0.23
	1.33	γ-fiber	6	12305	0.32
	1.67	γ-fiber	7	3631	0.93
	0.56	"Other" class	5	10104	0.27
	1.00	"Other" class	4	4454	0.39
	1.33	"Other" class	4	5265	0.52
	1.67	"Other" class	5	3091	0.73

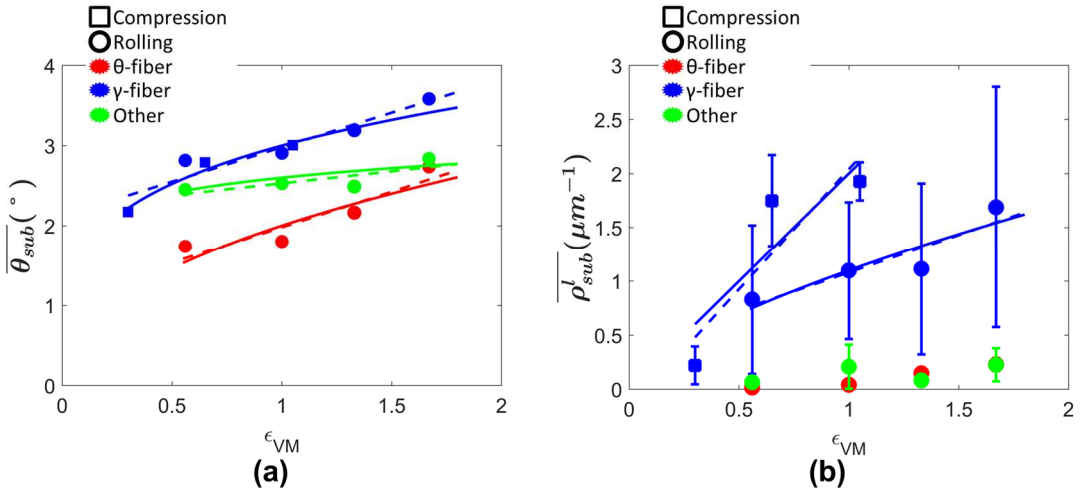

Fig. 11. Evolution of (a) $\overline{\theta_{sub}}$ and (b) $\overline{\rho^l_{sub}}$ with strain for each class of orientations. Represented standard deviations are weighted by the observed surface of each EBSD map. The dashed and full lines are least squares fits with linear and power laws of Eq. (1), (2) and (3) for $\overline{\theta_{sub}}$ and Eq. (4) and (5) for $\overline{\rho^l_{sub}}$.

The evolution of $\overline{\theta_{sub}}$ with strain for each class of orientations is illustrated in Fig. 11a. The orientation dependence of dislocation substructure development observed previously with ECCI technique is encountered again. Indeed, the subboundaries are more misoriented with increasing strain and the disorientation is always higher in the γ-fiber grains than in the grains of the two other classes. No saturation of the subboundaries' disorientation is observed in the present conditions. Deformation induced subboundaries can be classified into Incidental Dislocation Boundaries (IDBs) and Geometrically Necessary Boundaries (GNBs) [23]. For both of these boundaries, the disorientation angle increases with strain but in a distinct way. Pantleon proposed semi-empirical laws to describe the evolution of the disorientation angle for the two types of boundaries [61,62]. He applied these two laws on data obtained on cold rolled pure Al or Al alloy [12,63]. However, these laws might not be suitable to bcc materials because the fit with the present experimental data does not show satisfactory results. As a lower disorientation threshold is considered in the present case, the majority of IDBs are ignored. Consequently, the characterized subboundaries are probably GNBs. In the present case, least squares fits with a linear and a power law give suitable results:

- θ-fiber grains: $\overline{\theta_{sub}}\,(°) = 0.89\,\varepsilon_{VM} + 1.09$ or $\overline{\theta_{sub}}\,(°) = 2.02\,\varepsilon_{VM}^{0.45}$ (1)
- γ-fiber grains: $\overline{\theta_{sub}}\,(°) = 0.86\,\varepsilon_{VM} + 2.12$ or $\overline{\theta_{sub}}\,(°) = 3.04\,\varepsilon_{VM}^{0.25}$ (2)
- "Other"-oriented grains: $\overline{\theta_{sub}}\,(°) = 0.30\,\varepsilon_{VM} + 2.23$ or $\overline{\theta_{sub}}\,(°) = 2.56\,\varepsilon_{VM}^{0.11}$ (3)

The differences between these equations show clearly that there is no universal law to describe the evolution of the subboundaries disorientation for whatever crystallographic orientation. The power law coefficient is close to 0.5 for the θ-fiber grains (Eq. (1)) which corresponds to the law proposed by Pantleon [61,62] for IDBs. This result allows to speculate that dislocation subboundaries close to IDBs can appear in the θ-fiber grains, as already supposed in previous work [38]. Experimental results for higher strains are necessary in order to decide which type of law fits better: a linear or a power law.

On the other hand, more substructures are developed in the γ-fiber grains as shown in Fig. 11b. The quantity of subboundaries remains very low even for high strains for the grains of the two other classes of orientations. Focusing on the γ-fiber grains, $\overline{\rho_{sub}^{l}}$ shows distinct evolution between the compression case and the rolling case. For rolled samples, $\overline{\rho_{sub}^{l}}$ increases continuously with strain. For compressed samples, more subboundaries are developed in the γ-fiber grains and $\overline{\rho_{sub}^{l}}$ appears to quickly saturate around 2 μm^{-1} for $\varepsilon_{VM} \approx 0.65$. Higher strains obtained by compression would confirm this saturation. The present results for the compressed γ-fiber grains are consistent with those previously

reported for cold rolled pure nickel [64].The evolutions of the grain size for both cases are similar. This observation indicates that the different evolution of $\overline{\rho_{sub}^{l}}$ in the γ-fiber grains for compression and rolling is not because of subboundaries transforming into boundaries with disorientation angles higher than the upper threshold of 10°.

Besides, the development of dislocation substructures seems more homogeneous during the compression deformation than during the rolling deformation since the distribution of ρ_{sub}^{l} values spreads on larger range for the latter. Those two observations are probably related to the strong γ-fiber texture observed in the samples used for compression (Fig. 4a). Indeed, the γ-fiber grains represent between 70% and 80% of the initial state for the compressed samples and no more than 10% of the one for the rolled samples. Therefore, because of the crystal plasticity and the interactions between the different types of grains, the compressed samples present more homogeneous dislocation subboundaries with less spread as observed in Fig. 11b. This homogeneity is the probable reason behind the fast increase and the saturation of $\overline{\rho_{sub}^{l}}$ for the case of compressed samples. In the case of rolled samples, dislocations subboundaries continue to form even at high strains because of the heterogeneity of the subboundaries. Hutchinson reported on cold rolled steel [56] a similar impact of the neighboring environment on the grain deformation. The case of a “hard” grain with a high Taylor factor adjacent to a “soft” grain with a low Taylor factor was investigated. The hard grain, which has a higher flow stress, tends to resist deformation whereas the soft grain has to bend around this grain. This leads also to a weakening of the texture as the orientation of the soft grain will be spread. This case can be transposed to the present rolling case: γ-fiber grains are quite often surrounded by softer θ-fiber and “other”-oriented grains which will deform more easily as can be seen with EBSD maps of Appendix D.

As for $\overline{\theta_{sub}}$ previously, the evolution of $\overline{\rho_{sub}^{l}}$ with strain can be modelled. Considering the low values for θ-fiber and “other” grains, the modelling was only done for γ-fiber grains. Moreover, as the evolutions are different between compression and rolling cases, distinct laws were determined for each case. Least squares fits with a linear and a power law give suitable results:

- Compressed γ-fiber grains: $\overline{\rho_{sub}^{l}}\ (\mu m^{-1}) = 2{,}23\ \varepsilon_{VM} - 0{,}19$ or $\overline{\rho_{sub}^{l}}\ (\mu m^{-1}) = 2{,}00\ \varepsilon_{VM}^{1{,}01}$ (4)
- Rolled γ-fiber grains: $\overline{\rho_{sub}^{l}}\ (\mu m^{-1}) = 0{,}70\ \varepsilon_{VM} + 0{,}38$ or $\overline{\rho_{sub}^{l}}\ (\mu m^{-1}) = 1{,}10\ \varepsilon_{VM}^{0{,}66}$ (5)

Values of $\overline{\rho_{sub}^{l}}$ can be related to the substructure sizes with stereographic considerations and with the hypothesis that the substructures are spheres, have all the same size and are uniformly distributed along the surface [65,66]. Thus, the average sizes can be determined with the following equation:

$$\overline{d_{sub}} = \frac{2}{3}\,\pi\,\frac{1}{\overline{\rho_{sub}^{l}}} \quad (6)$$

where $\overline{d_{sub}}$ is the average substructure equivalent diameter (µm) and $\overline{\rho_{sub}^{l}}$ is the average linear density of subboundaries (µm^{-1}).

This calculation was performed only for γ-fiber grains because values of $\overline{\rho_{sub}^{l}}$ were very low (the hypothesis of uniform distribution is not valid) for the other grains and led to non-physical substructure sizes of several tens of µm. For the same reason, the first strain for the compression case ($\varepsilon_{VM} \approx 0.30$) was not considered so only the rolling case was modelled. Least squares fits of experimental points with a linear and a power law give correct results:

- Rolled γ-fiber grains: $\overline{d_{sub}}\ (\mu m) = -1.06\ \varepsilon_{VM} + 3.10$ or $\overline{d_{sub}}\ (\mu m) = 1.90\ \varepsilon_{VM}^{-0.51}$ (7)

4.3.3. Long-range orientation gradients analysis

Although no subboundaries (abrupt disorientations) are clearly formed in the θ-fiber grains in the ECCI micrographs (Fig. 9c and d and Fig. 10c and d), orientation contrasts are observed in these grains with progressive transitions from white to black regions and might imply the presence of long-range orientation gradients. The softer θ-fiber grains are prone to be subject to internal bending due to the neighboring grains with different deformation behaviors inducing long-range orientation gradients. As observed on cold rolled pure tantalum [67], the θ-fiber grains can even split due to the interaction with neighboring γ-fiber grains. In contrast, in the γ-fiber grains, the disorientations across subboundaries tend to alternate with no significant long-range orientation gradient as observed on cold rolled pure aluminum [36].

For the analysis of orientation gradients, EBSD maps of Table 1 were used. Disorientation profiles passing through the center of the map at every 3° were plotted for each EBSD map (i.e. 60 profiles per map). The evolution of the disorientation along each profile was least squares fitted with a linear law and the slope was considered as the orientation gradient. Since there is no guarantee that one of the profiles is in the same direction as the highest orientation gradient, the maximal value was considered as the closest one to the real orientation gradient (this value underestimates the real orientation gradient). For each case of Table 1, the average value (weighted by the surface of EBSD map) of the estimated orientation gradient is calculated (see the right column of Table 1).

For each class of orientations, the average orientation gradient increases with strain as expected. Long-range orientation gradients tend to develop continuously with strain in θ-fiber grains whereas in γ-fiber grains gradients become more significant for high strain ($\varepsilon_{VM} \approx 1.67$), which might reveal a beginning of grain fragmentation. Therefore, although

orientation gradients are more apparent in θ-fiber grains with the ECCI micrographs (Fig. 9c and d and Fig. 10c and d), they are not higher than the ones in γ-fiber grains. Moreover, orientation gradients in γ-fiber grains appear to be higher for the rolling case than for the compression case. This difference is most probably due to the more varied neighborhood of γ-fiber grains in rolled samples.

5. Conclusion

In this study, a quantitative analysis of cold deformed pure tantalum microstructure is presented. Two deformation modes, compression and rolling, each applied on a different initial state were employed to access the influence of crystallographic orientation. The orientation dependence of deformation was emphasized with two different scales of observation with SEM. The following conclusions can be drawn from the present analysis:

- During compression, the γ-fiber seems to be stable. For the case of rolling, the friction causing shear components leads to a decrease in the γ-fiber fraction.
- At grain scale, intragranular heterogeneities were evaluated with the dislocation density ρ_{EBSD}. γ-fiber grains have always higher values than θ-fiber and "other"-oriented grains. At this scale, there is no significant difference in ρ_{EBSD} values between compressed and rolled γ-fiber grains.
- At dislocation substructure scale, this orientation dependence was also pointed out with developed substructures in the interior of γ-fiber grains and almost no substructures in the θ-fiber grains. Quantitative characterization of substructure development was performed and models describing the evolution of the average disorientation and size of substructures were proposed for the γ-fiber grains. At this scale, the difference of substructure development between compressed and rolled γ-fiber grains is significant.
- When the γ-fiber is weakly present (no more than 30% for the rolling case), the substructure development is quite heterogeneous and the substructure disorientation and size increase continuously with increasing strain. However, when the γ-fiber is dominant (more than 65% for the compression case), a very fast saturation of subboundaries density was observed. In such conditions, subboundaries are formed for small strains and only their disorientation increases for further strains.
- Intragranular orientation gradients were analyzed. For the rolling case, long-range orientation gradients tend to develop continuously with strain in θ-fiber grains whereas in γ-fiber grains gradients become substantial for high strain ($\varepsilon_{VM} \approx 1.67$).

For both cases the orientation gradients were very close. Orientation gradients in γ-fiber grains are higher in rolled samples than in compressed samples as the neighborhood of γ-fiber grains is more varied for the former case.

One of the main conclusions of the present work is that describing the deformed microstructure through dislocation density is not enough. Therefore, in order to study and model thermally activated physical mechanisms driven by stored energy induced by dislocations, like recovery and recrystallization, it is necessary to quantify dislocation substructures.

Acknowledgments

Cyrille Collin, Gilbert Fiorucci, Suzanne Jacomet and Gabriel Monge are acknowledged for their help in performing sample preparation, deformation experiments, microscopy analyzes and XRD characterization respectively. The authors are also very grateful to Rémy Besnard for his long contribution to this research program between CEMEF and CEA DAM Valduc and to CEA DAM Valduc for funding.

Data availability

The raw/processed data required to reproduce these findings cannot be shared at this time as the data also forms part of an ongoing study.

References

[1] Humphreys FJ, Hatherly M. Recrystallization and Related Annealing Phenomena 2nd Edition. Elsevier. 2004.

[2] Bréchet YJ, Zurob HS, Hutchinson CR. On the effect of pre-recovery on subsequent recrystallization. Int J Mater Res 2009;100:1446–1448.

[3] Liu SF, Liu YH, Li LJ, Deng C, Fan HY, Guo Y, et al. Effects of pre-recovery on the recrystallization microstructure and texture of high-purity tantalum. J Mater Sci 2018;53:2985–94. https://doi.org/10.1007/s10853-017-1732-z.

[4] Polak C. Métallurgie et recyclage du niobium et du tantale. Tech Ing Métallurgie Extr 2009;TIB369DUO.

[5] Buckman RW. New applications for tantalum and tantalum alloys. JOM 2000;52:40–1. https://doi.org/10.1007/s11837-000-0100-6.
[6] Cardonne SM, Kumar P, Michaluk CA, Schwartz HD. Tantalum and its alloys. Int J Refract Met Hard Mater 1995;13:187–94. https://doi.org/10.1016/0263-4368(95)94023-R.
[7] Hull D, Bacon DJ. Chapter 6 - Dislocations in Other Crystal Structures. In: Hull D, Bacon DJ, editors. Introd. Dislocations Fifth Ed., Oxford: Butterworth-Heinemann; 2011, p. 109–36. https://doi.org/10.1016/B978-0-08-096672-4.00006-2.
[8] Weinberger CR, Boyce BL, Battaile CC. Slip planes in bcc transition metals. Int Mater Rev 2013;58:296–314. https://doi.org/10.1179/1743280412Y.0000000015.
[9] Pegel B. Stacking Faults on 110 Planes in the B.C.C. Lattice. Phys Status Solidi B 1968;28:603–9. https://doi.org/10.1002/pssb.19680280218.
[10] Wasilewski RJ. B.C.C. stacking fault energies. Scr Metall 1967;1:45–7. https://doi.org/10.1016/0036-9748(67)90012-9.
[11] Furu T, Ørsund R, Nes E. Subgrain growth in heavily deformed aluminium—experimental investigation and modelling treatment. Acta Metall Mater 1995;43:2209–32. https://doi.org/10.1016/0956-7151(94)00410-2.
[12] Hughes DA, Liu Q, Chrzan DC, Hansen N. Scaling of microstructural parameters: Misorientations of deformation induced boundaries. Acta Mater 1997;45:105–12. https://doi.org/10.1016/S1359-6454(96)00153-X.
[13] Liu Q, Hansen N. Geometrically necessary boundaries and incidental dislocation boundaries formed during cold deformation. Scr Metall Mater 1995;32:1289–95. https://doi.org/10.1016/0956-716X(94)00019-E.
[14] Mishin OV, Juul Jensen D, Hansen N. Microstructures and boundary populations in materials produced by equal channel angular extrusion. Mater Sci Eng A 2003;342:320–8. https://doi.org/10.1016/S0921-5093(02)00311-8.
[15] Hughes DA, Chrzan DC, Liu Q, Hansen N. Scaling of Misorientation Angle Distributions. Phys Rev Lett 1998;81:4664–7. https://doi.org/10.1103/PhysRevLett.81.4664.
[16] Hughes DA, Hansen N. Microstructure and strength of nickel at large strains. Acta Mater 2000;48:2985–3004. https://doi.org/10.1016/S1359-6454(00)00082-3.
[17] Hu H. Reorientation in recrystallization: origin of cube grains in copper -- a study of nucleation of recrystallization. Textures Res. Pract. Springer, 1969, p. 200.
[18] Gil Sevillano J, van Houtte P, Aernoudt E. Large strain work hardening and textures. Prog Mater Sci 1980;25:69–134. https://doi.org/10.1016/0079-6425(80)90001-8.
[19] Thompson SJ, Flewitt PEJ. The defect structure and superconducting transition of cold-worked niobium. J Common Met 1975;40:269–83. https://doi.org/10.1016/0022-5088(75)90071-5.

[20] Langford G, Cohen M. Strain hardening of iron by severe plastic deformation. Trans ASM 1969;62:623–38.
[21] Hansen N, Hughes DA. Analysis of large dislocation populations in deformed metals. Phys Status Solidi A 1995;149:155–72. https://doi.org/10.1002/pssa.2211490111.
[22] Hughes DA, Hansen N. High angle boundaries formed by grain subdivision mechanisms. Acta Mater 1997;45:3871–86. https://doi.org/10.1016/S1359-6454(97)00027-X.
[23] Kuhlmann-Wilsdorf D, Hansen N. Geometrically necessary, incidental and subgrain boundaries. Scr Metall Mater 1991;25:1557–62. https://doi.org/10.1016/0956-716X(91)90451-6.
[24] Pantleon W, Hansen N. Dislocation boundaries—the distribution function of disorientation angles. Acta Mater 2001;49:1479–93. https://doi.org/10.1016/S1359-6454(01)00027-1.
[25] Pantleon W. On the apparent saturation of the average disorientation angle with plastic deformation. Scr Mater 2005;53:757–62. https://doi.org/10.1016/j.scriptamat.2005.05.007.
[26] He W, Ma W, Pantleon W. Microstructure of individual grains in cold-rolled aluminium from orientation inhomogeneities resolved by electron backscattering diffraction. Mater Sci Eng A 2008;494:21–7. https://doi.org/10.1016/j.msea.2007.10.092.
[27] Humphreys FJ. Review Grain and subgrain characterisation by electron backscatter diffraction. J Mater Sci 2001;36:3833–54. https://doi.org/10.1023/A:1017973432592.
[28] Hurley PJ, Humphreys FJ. The application of EBSD to the study of substructural development in a cold rolled single-phase aluminium alloy. Acta Mater 2003;51:1087–102. https://doi.org/10.1016/S1359-6454(02)00513-X.
[29] Lanjewar H, Naghdy S, Vercruysse F, Kestens LAI, Verleysen P. Severe plastically deformed commercially pure aluminum: Substructure, micro-texture and associated mechanical response during uniaxial tension. Mater Sci Eng A 2019;764:138195. https://doi.org/10.1016/j.msea.2019.138195.
[30] Sandim HRZ, Raabe D. EBSD study of grain subdivision of a Goss grain in coarse-grained cold-rolled niobium. Scr Mater 2005;53:207–12. https://doi.org/10.1016/j.scriptamat.2005.03.045.
[31] Moussa C, Bernacki M, Besnard R, Bozzolo N. About quantitative EBSD analysis of deformation and recovery substructures in pure Tantalum. IOP Conf. Ser. Mater. Sci. Eng., vol. 89, IOP Publishing; 2015, p. 012038.
[32] Moussa C, Bernacki M, Besnard R, Bozzolo N. Statistical analysis of dislocations and dislocation boundaries from EBSD data. Ultramicroscopy 2017;179:63–72. https://doi.org/10.1016/j.ultramic.2017.04.005.

671 [33] Dillamore IL, Smith CJE, Watson TW. Oriented Nucleation in the Formation of
672 Annealing Textures in Iron. Met Sci J 1967;1:49–54.
673 https://doi.org/10.1179/msc.1967.1.1.49.
674 [34] Every RL, Hatherly M. Oriented Nucleation in Low-Carbon Steels. Texture
675 1974;1:380237. https://doi.org/10.1155/TSM.1.183.
676 [35] Borbély A, Driver JH, Ungár T. An X-ray method for the determination of stored
677 energies in texture components of deformed metals; application to cold worked ultra
678 high purity iron. Acta Mater 2000;48:2005–16. https://doi.org/10.1016/S1359-
679 6454(99)00457-7.
680 [36] Liu Q, Juul Jensen D, Hansen N. Effect of grain orientation on deformation structure in
681 cold-rolled polycrystalline aluminium. Acta Mater 1998;46:5819–38.
682 https://doi.org/10.1016/S1359-6454(98)00229-8.
683 [37] Sandim HRZ, Martins JP, Padilha AF. Orientation effects during grain subdivision and
684 subsequent annealing in coarse-grained tantalum. Scr Mater 2001;45:733–8.
685 https://doi.org/10.1016/S1359-6462(01)01087-9.
686 [38] Deng C, Liu SF, Hao XB, Ji JL, Zhang ZQ, Liu Q. Orientation dependence of stored
687 energy release and microstructure evolution in cold rolled tantalum. Int J Refract Met
688 Hard Mater 2014;46:24–9. https://doi.org/10.1016/j.ijrmhm.2014.05.005.
689 [39] Lin N, Liu S, Liu Y, Fan H, Zhu J, Deng C, et al. Effects of asymmetrical rolling on
690 through-thickness microstructure and texture of body-centered cubic (BCC) tantalum.
691 Int J Refract Met Hard Mater 2019;78:51–60.
692 https://doi.org/10.1016/j.ijrmhm.2018.08.012.
693 [40] Liu Y, Liu S, Deng C, Fan H, Yuan X, Liu Q. Inhomogeneous deformation of {111} grain
694 in cold rolled tantalum. J Mater Sci Technol 2018;34:2178–82.
695 https://doi.org/10.1016/j.jmst.2018.03.015.
696 [41] Yu T, Hansen N, Huang X. Linking recovery and recrystallization through triple junction
697 motion in aluminum cold rolled to a large strain. Acta Mater 2013;61:6577–86.
698 https://doi.org/10.1016/j.actamat.2013.07.040.
699 [42] Bachmann F, Hielscher R, Schaeben H. Grain detection from 2d and 3d EBSD data—
700 Specification of the MTEX algorithm. Ultramicroscopy 2011;111:1720–33.
701 https://doi.org/10.1016/j.ultramic.2011.08.002.
702 [43] Clark JB, Garrett RK, Jungling TL, Vandermeer RA, Vold CL. Effect of processing
703 variables on texture and texture gradients in tantalum. Metall Trans A 1991;22:2039–48.
704 https://doi.org/10.1007/BF02669871.
705 [44] Truszkowski W, Kr'ol J, Major B. Inhomogeneity of rolling texture in fcc metals. Metall
706 Trans A 1980;11:749–58. https://doi.org/10.1007/BF02661204.

[45] Kerisit C. Analyse des mécanismes de recristallisation statique du tantale déformé à froid pour une modélisation en champ moyen. Thèse. Ecole Nationale Supérieure des Mines de Paris, 2012.
[46] Dieter GE. Mechanical metallurgy. SI Metric Edition. McGraw-Hill Book Company; 1988.
[47] Asbeck HO, Mecking H. Influence of friction and geometry of deformation on texture inhomogeneities during rolling of Cu single crystals as an example. Mater Sci Eng 1978;34:111–9. https://doi.org/10.1016/0025-5416(78)90041-1.
[48] Dillamore IL, Katoh H, Haslam K. The Nucleation of Recrystallisation and the Development of Textures in Heavily Compressed Iron-Carbon Alloys. Texture 1974;1:212564. https://doi.org/10.1155/TSM.1.151.
[49] Wilkinson AJ. Deformation Textures. In: Buschow KHJ, Cahn RW, Flemings MC, Ilschner B, Kramer EJ, Mahajan S, et al., editors. Encycl. Mater. Sci. Technol., Oxford: Elsevier; 2001, p. 2022–6. https://doi.org/10.1016/B0-08-043152-6/00368-5.
[50] Raabe D, Schlenkert G, Weisshaupt H, Lücke K. Texture and microstructure of rolled and annealed tantalum. Mater Sci Technol 1994;10:299–305. https://doi.org/10.1179/mst.1994.10.4.299.
[51] Ashby MF. The deformation of plastically non-homogeneous materials. Philos Mag J Theor Exp Appl Phys 1970;21:399–424. https://doi.org/10.1080/14786437008238426.
[52] Pantleon W. Resolving the geometrically necessary dislocation content by conventional electron backscattering diffraction. Scr Mater 2008;58:994–7. https://doi.org/10.1016/j.scriptamat.2008.01.050.
[53] Seret A, Moussa C, Bernacki M, Signorelli J, Bozzolo N. Estimation of geometrically necessary dislocation density from filtered EBSD data by a local linear adaptation of smoothing splines. J Appl Crystallogr 2019;52:548–63. https://doi.org/10.1107/S1600576719004035.
[54] Nye JF. Some geometrical relations in dislocated crystals. Acta Metall 1953;1:153–62. https://doi.org/10.1016/0001-6160(53)90054-6.
[55] Godfrey A, Mishin OV, Yu T. Characterization and influence of deformation microstructure heterogeneity on recrystallization. IOP Conf Ser Mater Sci Eng 2015;89:012003. https://doi.org/10.1088/1757-899X/89/1/012003.
[56] Hutchinson B. Deformation microstructures and textures in steels. Philos Trans R Soc Math Phys Eng Sci 1999;357:1471–85. https://doi.org/10.1098/rsta.1999.0385.
[57] Sandim HRZ, Martins JP, Pinto AL, Padilha AF. Recrystallization of oligocrystalline tantalum deformed by cold rolling. Mater Sci Eng A 2005;392:209–21. https://doi.org/10.1016/j.msea.2004.09.032.
[58] Hansen LT. Characterization of Dislocation - Grain Boundary Interactions Through Electron Backscatter Diffraction. Brigham Young University, 2019.

[59] Rajmohan N, Hayakawa Y, Szpunar JA, Root JH. Neutron diffraction method for stored energy measurement in interstitial free steel. Acta Mater 1997;45:2485–94. https://doi.org/10.1016/S1359-6454(96)00371-0.

[60] Takayama Y, Szpunar JA. Stored Energy and Taylor Factor Relation in an Al-Mg-Mn Alloy Sheet Worked by Continuous Cyclic Bending. Mater Trans 2004;45:2316–25. https://doi.org/10.2320/matertrans.45.2316.

[61] Pantleon W. The evolution of disorientations for several types of boundaries. Mater Sci Eng A 2001;319–321:211–5. https://doi.org/10.1016/S0921-5093(01)00947-9.

[62] Pantleon W. Stage IV work-hardening related to disorientations in dislocation structures. Mater Sci Eng A 2004;387–389:257–61. https://doi.org/10.1016/j.msea.2003.11.088.

[63] Liu Q, Huang X, Lloyd DJ, Hansen N. Microstructure and strength of commercial purity aluminium (AA 1200) cold-rolled to large strains. Acta Mater 2002;50:3789–802. https://doi.org/10.1016/S1359-6454(02)00174-X.

[64] Hughes DA, Hansen N. The microstructural origin of work hardening stages. Acta Mater 2018;148:374–83. https://doi.org/10.1016/j.actamat.2018.02.002.

[65] DeHoff RT. Problem Solving Using Quantitative Stereology. In: Vander Voort GF, editor. Appl. Metallogr., Boston, MA: Springer US; 1986, p. 89–99. https://doi.org/10.1007/978-1-4684-9084-8_7.

[66] Underwood EE. Quantitative Stereology for Microstructural Analysis. In: McCall JL, Mueller WM, editors. Microstruct. Anal. Tools Tech., Boston, MA: Springer US; 1973, p. 35–66. https://doi.org/10.1007/978-1-4615-8693-7_3.

[67] Zhu J, Liu S, Long D, Orlov D, Liu Q. Pass number dependence of through-thickness microstructure homogeneity in tantalum sheets under the change of strain path. Mater Charact 2020;160:110076. https://doi.org/10.1016/j.matchar.2019.110076.

Appendices

Appendix A: Variations of texture at the center of the initial sheet

The different distributions of γ-fiber between EBSD and XRD techniques (Fig. 2d) and also between the two geometries of compression samples (Fig. 4) might stem from spatial heterogeneities. In order to verify this possibility, the microstructure at the center of the initial sheet was characterized in the plane radial direction RD/transverse direction TD as illustrated in Fig. A.1. Three EBSD maps ten times larger than the ones used in this study (Fig. 1a for example) were performed at three different random locations with an acquisition step size of 3.45 µm over a rectangular area of 3.80 mm × 2.85 mm.

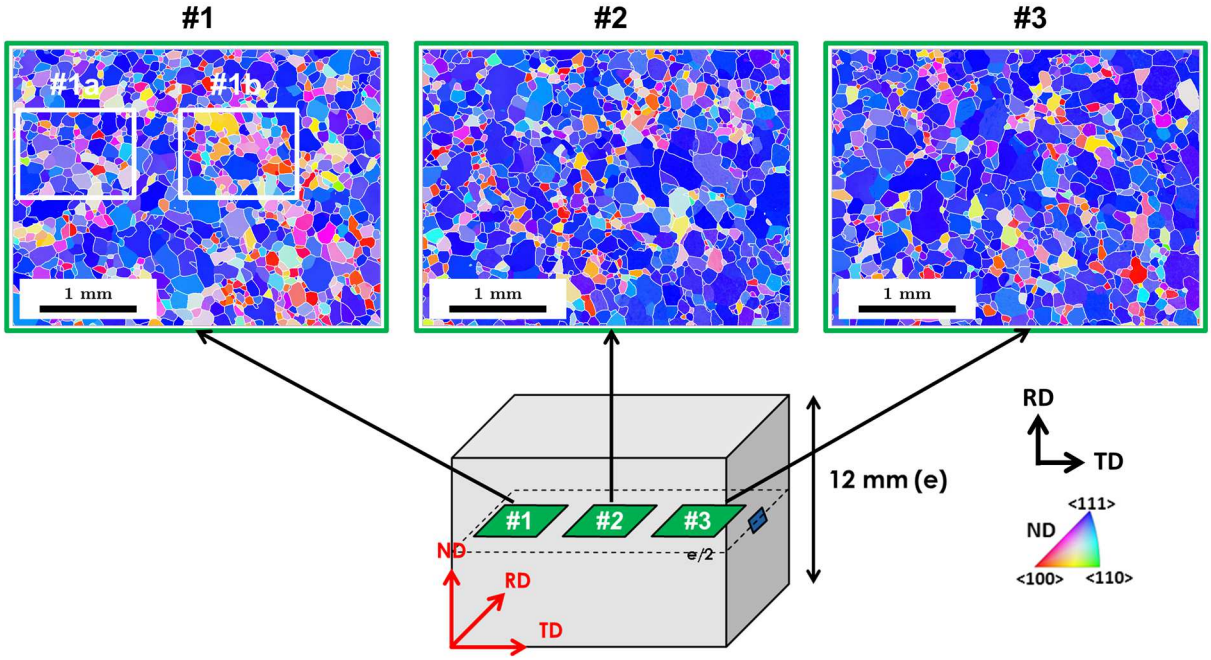

Fig. A.1. EBSD orientation maps acquired at the center of the initial sheet (ND projected onto the standard triangle). Grain boundaries are plotted in white lines (10° disorientation angle threshold). Schematic blue rectangle on the right side of the schema and white rectangles on EBSD map #1 represent the EBSD map size used in this study as the one of Fig. 1a.

The respective surface fraction of θ-fiber grains, γ-fiber grains and “other” grains for each EBSD map are detailed quantitatively in Fig. A.2. Results confirm the preponderance of the γ-fiber at the center of the initial sheet with higher statistical relevance but show also that its fraction varies between 70% and 80% depending on the location of EBSD map. White rectangles on the EBSD map #1 (denoted as maps #1a and #1b) represent the size of EBSD maps performed for intergranular analysis in the present study. It appears clearly that the γ-fiber can be much less dominant with this size of observation as presented in Fig. A.2.

790 Indeed, the intensity of γ-fiber is around 70% in the left EBSD map #1a whereas it is around
791 50% in the right EBSD map #1b. These non-negligible variations of texture can explain the
792 differences observed between the two geometries of compression samples as the samples
793 were taken from distant regions in the initial sheet.

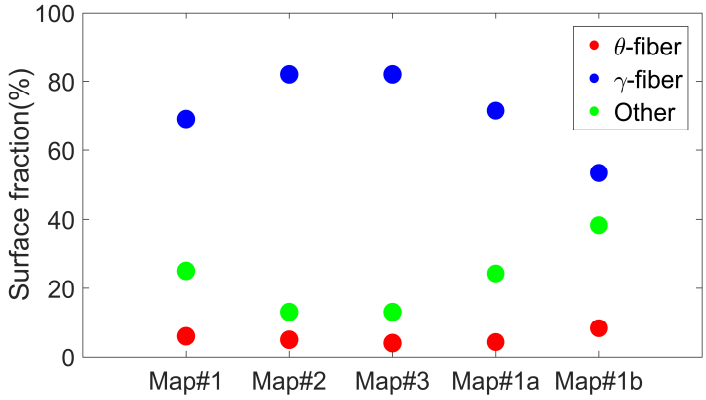

794

795 Fig. A.2. Evolution of θ-fiber, γ-fiber and “other” orientations for each EBSD map of Fig. A.1.

Appendix B: EBSD orientation maps acquired on the geometry 1 double-cone compression sample

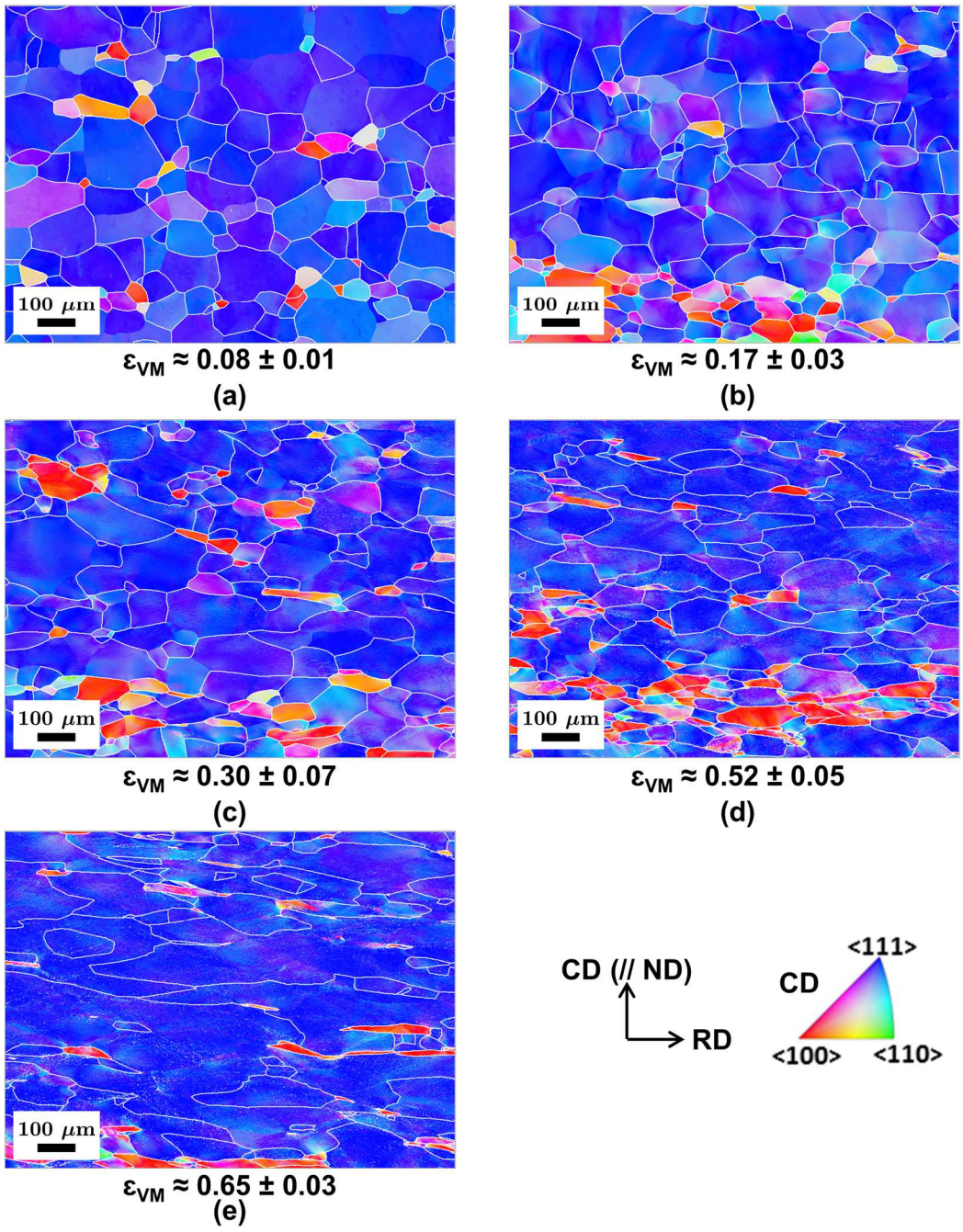

Fig. B.1. EBSD orientation maps of samples deformed by compression with geometry 1 at equivalent plastic strains of (a) 0.08, (b) 0.17, (c) 0.30, (d) 0.52 and (e) 0.65 respectively (CD projected onto the standard triangle). Grain boundaries are plotted in white lines (10° disorientation angle threshold).

Appendix C: EBSD orientation maps acquired on the geometry 2 double-cone compression sample

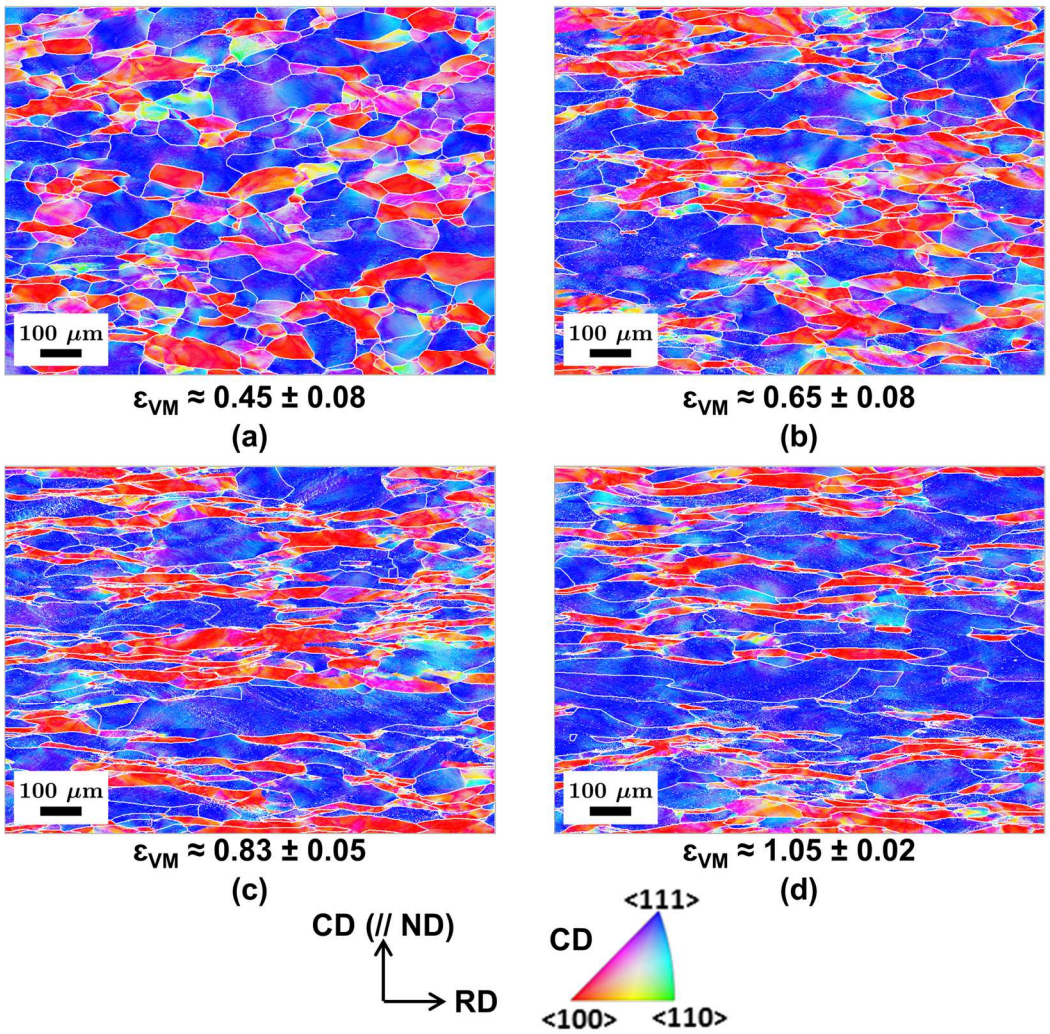

Fig. C.1. EBSD orientation maps of samples deformed by compression with geometry 2 at equivalent plastic strains of (a) 0.45, (b) 0.65, (c) 0.83, (d) 1.05 respectively (CD projected onto the standard triangle). Grain boundaries are plotted in white lines (10° disorientation angle threshold).

Appendix D: EBSD orientation maps acquired on rolled samples

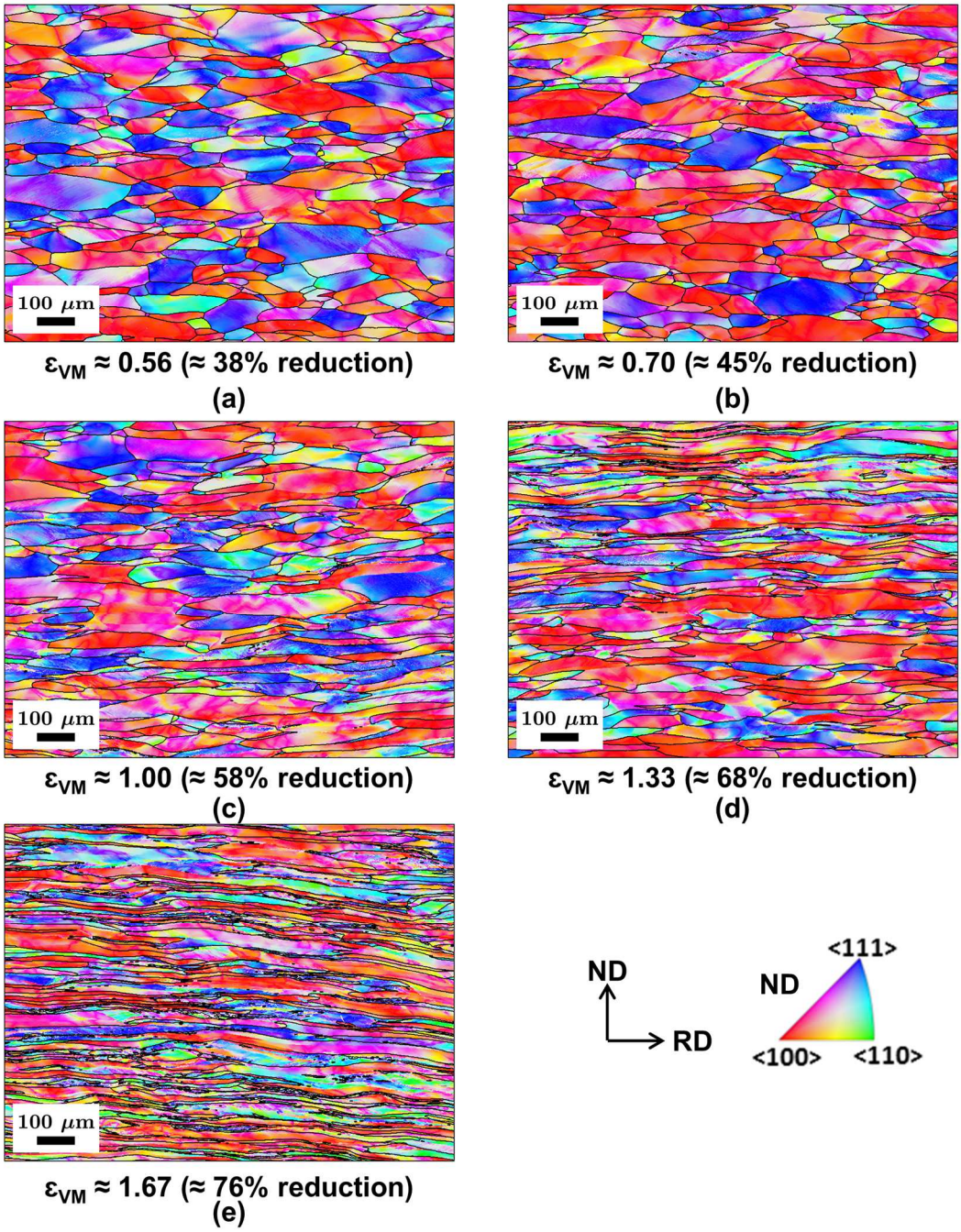

Fig. D.1. EBSD orientation maps of samples deformed by rolling at equivalent plastic strains of (a) 0.56, (b) 0.70, (c) 1.00, (d) 1.33 and (e) 1.67 respectively (ND projected onto the standard triangle). Grain boundaries are plotted in black lines (10° disorientation angle threshold).